Research article

Ting Hu[a,]*, Qize Zhong[a], Nanxi Li, Yuan Dong, Zhengji Xu, Yuan Hsing Fu, Dongdong Li, Vladimir Bliznetsov, Yanyan Zhou, Keng Heng Lai, Qunying Lin, Shiyang Zhu and Navab Singh

CMOS-compatible a-Si metalenses on a 12-inch glass wafer for fingerprint imaging

https://doi.org/10.1515/nanoph-2019-0470
Received November 17, 2019; revised January 24, 2020; accepted January 26, 2020

Abstract: Metalenses made of artificial sub-wavelength nanostructures have shown the capability of light focusing and imaging with a miniaturized size. Here, we report the demonstration of mass-producible amorphous silicon metalenses on a 12-inch glass wafer via the complementary metal-oxide-semiconductor compatible process. The measured numerical aperture of the fabricated metalens is 0.496 with a focusing spot size of 1.26 μm at the wavelength of 940 nm. The metalens is applied in an imaging system to test the imaging resolution. The minimum bar of the resolution chart with a width of 2.19 μm is clearly observed. Furthermore, the same system demonstrates the imaging of a fingerprint, and proofs the concept of using metalens array to reduce the system size for future compact consumer electronics.

Keywords: metasurface; glass wafer; metalens.

1 Introduction

Metasurfaces composed of quasi-periodic sub-wavelength nanostructures have attracted a lot of research interest recently, as they can be artificially designed to tailor the wavefront of light in the sub-wavelength scale. By engineering the phase and the amplitude of electromagnetic waves, miniature-sized flat optic components with various functionalities have been demonstrated [1, 2]. Among these components, the metalens has drawn significant attention due to its wide applications. Metalenses based on plasmonic resonance in nanometallic structures were firstly demonstrated to work in the visible and near-infrared wavelength regimes [3–5]. Though the metallic antenna can be made as thin as 30 nm, the focusing efficiency is low due to its high optical loss. In order to improve the lens performance, researchers have gradually moved the focus to dielectric metasurfaces [6–24]. The amorphous silicon (a-Si) is commonly used for devices working at the near-infrared wavelength regime due to its low optical loss [7–12], while for the visible wavelength regime, silica, titanium dioxide (TiO_2), gallium nitride (GaN), and silicon nitride (SiN) are appropriate materials [13–20]. There are a few works choosing silicon as the material for metalenses at the visible wavelength [21, 22]; however, these lenses have a relatively low focusing efficiency even with a very thin antenna layer. Furthermore, except for the works reported in Refs. [12, 13], to the best of our knowledge, most of the metalenses demonstrated thus far are patterned using electron beam lithography, which requires long patterning time for large-scale nanostructures and hence is not suitable for mass production. Although in Refs. [12, 13], ultraviolet (UV) lithography was used to pattern the metalenses on a 4-inch glass wafer, the limited resolution hindered it from obtaining good-performance metalenses for shorter wavelengths of <1 μm. Lenses working at short wavelengths are essential components in consumer electronics, such as smartphones. One typical application is the optical module for fingerprint imaging. Conventional lenses based on optical refraction suffers from small numerical apertures (NAs) and bulky size, which cannot meet the demands of thinner optical modules for fingerprint imaging. Recently, the wafer-level Fresnel microlens array fabricated by nanoimprint technology to realize compact fingerprint capturing was

[a]**Ting Hu and Qize Zhong:** These authors contributed equally to this work.
***Corresponding author: Ting Hu,** Institute of Microelectronics, Agency for Science Technology and Research (A*STAR), 2 Fusionopolis Way, #08-02, Innovis, Singapore 138634, Singapore, e-mail: hut@ime.a-star.edu.sg. https://orcid.org/0000-0002-7134-1748
Qize Zhong, Nanxi Li, Yuan Dong, Zhengji Xu, Yuan Hsing Fu, Dongdong Li, Vladimir Bliznetsov, Yanyan Zhou, Keng Heng Lai, Qunying Lin, Shiyang Zhu and Navab Singh: Institute of Microelectronics, Agency for Science Technology and Research (A*STAR), 2 Fusionopolis Way, #08-02, Innovis, Singapore 138634, Singapore. https://orcid.org/0000-0002-0524-0949 (N. Li); https://orcid.org/0000-0002-4024-0469 (Y. Dong). https://orcid.org/0000-0002-0265-6228 (Z. Xu). https://orcid.org/0000-0002-7691-0196 (Y.H. Fu)

Open Access. © 2020 Ting Hu et al., published by De Gruyter. This work is licensed under the Creative Commons Attribution 4.0 Public License.

reported [25]. However, the grayscale lithograph was used in mold making, which increased the process complexity.

In this paper, we demonstrate an a-Si metalens working at 940 nm fabricated on a 12-inch glass wafer. The 193-nm ArF deep UV (DUV) immersion lithography is used to pattern our design with critical dimension as small as 100 nm. Different from our earlier work [26–29] based on a 12-inch silicon wafer, the glass wafer is used here, which is difficult to detect or handle by litho and etching tools. In order to solve this issue, a layer transfer process is used for metalens fabrication [30, 31]. The performance of the fabricated metalens is characterized by measuring its NA, focal-spot size, and focusing efficiency. The experimental results agree well with the three-dimensional (3D) finite-difference time-domain (FDTD) simulation. The metalens is then applied in an imaging system with the 1951 US Air Force (USAF) resolution chart as object. A clear image of a 2.19-μm-wide bar in the resolution chart is obtained. The same imaging system with the metalens is used for fingerprint imaging. As a proof-of-concept demonstration, the physical location of the single metalens is programmed to demonstrate the function of a metalens array, proofing the idea of reducing the system size for compact consumer electronics.

2 Device design and simulation

The schematic structure of the metalens design is shown in Figure 1A. It is constructed by sub-wavelength-sized a-Si cylindrical pillars fabricated on a glass substrate and embedded within an interlayer. The interlayer of siloxane, with a thickness of 60 μm, is induced during the layer transfer process to solve the glass wafer handling issue mentioned earlier. On top of the Si pillars, there is a 1-μm-thick silicon dioxide (SiO_2) cap layer. Panels B and C of Figure 1 show the side and top view of the meta-element, respectively. The a-Si pillar height is 600 nm, with a fixed edge-to-edge gap of 200 nm to its neighboring pillars. To focus the collimated incident light, the relative phase profile of the meta-elements needs to follow the spatial distribution below [16]:

$$\varphi(x, y) = 2\pi - \frac{2\pi}{\lambda}\left(\sqrt{x^2 + y^2 + f^2} - f\right), \tag{1}$$

where λ is the designed wavelength and f is the focal length. The position of the a-Si pillars is described by x and y. The phase shift of each building block can be adjusted by changing the diameter of the pillar. Through the 3D-FDTD simulation (FDTD Solutions, Lumerical Inc., Vancouver, British Columbia, Canada), the phase shift and the transmission of the a-Si pillar with respect to its diameter are shown in Figure 1D. Starting from the 100-nm diameter, the relative phase increases with larger diameters and reaches 2π at 294 nm. Meanwhile, the transmission is >0.94 when the diameter is <290 nm. From 290 to 294 nm, there is a drop in the transmission caused by resonance in the pillars. However, it should not have a significant effect on the metalens performance, as the 4-nm range is small compared with the whole diameter range from 100 to 294 nm. In the simulation, the mesh accuracy level 8 is selected, with the grid size of ~7 nm in both x and y directions and ~30 nm in the z direction. The periodic boundary is adopted for the computing region in the x and y directions, while the perfect matched layer boundary is chosen in z direction. The optical wavelength is set to be 940 nm. The height of the a-Si pillars is chosen to be 600 nm, and the refractive index of the interlayer and a-Si at 940 nm is set as 1.451 (the same with the cap SiO_2 layer) and 3.806, respectively.

Based on the phase shift obtained from the simulation (Figure 1D) together with the spatial distribution of

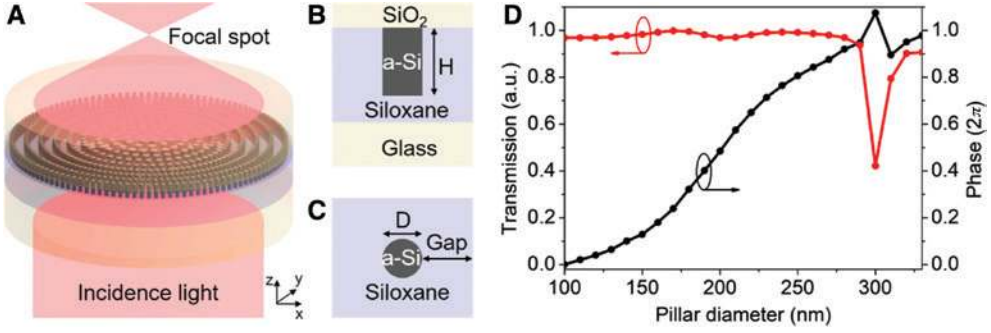

Figure 1: Schematic and unit cell design of the a-Si metalens.
(A) Schematic of the metalens. (B) Side view and (C) top view of the metalens unit cell. (D) Simulated phase shift and transmission profile with respect to the pillar diameter. The arrows indicate the corresponding y-axis of the data line.

the phase profile described in Eq. (1), the a-Si pillars are placed accordingly with a radial sampling distribution to construct a metalens in the 3D-FDTD simulation. The original designed diameter of the metalens is 2 mm; however, the 3D-FDTD simulation of such a large size requires a huge computing resource. Therefore, the diameter of the metalens is scaled down to 20 μm with the scaling factor of 100 in simulation. Such simulation is set up as an analogy to investigate the performance of the original designed metalens. In order to further reduce the simulation time, a relative lower mesh accuracy of 2 is selected, with the grid size of ~25 nm in x and y directions and ~100 nm in the z direction. The perfect matched layer boundary is adopted for the computing region in all of the x, y, and z directions. For the NA of 0.5, the simulated metalens is expected to have a focal length of 17.32 μm. The electric field intensity (E-intensity) in the light propagation plane (xz plane) and the E-intensity at the focal plane (xy plane) are shown Figure 2A and B, respectively. In Figure 2A, the spatial convergence of the incident plane wave can be observed after passing through the metalens located at $z = 0$ μm. The incident wave is focused at $z = 17.32$ μm, as expected for the NA of 0.5. Figure 2B shows the E-intensity distribution at the cross section of the focal plane, from which the focusing spot size and the efficiency can be obtained. Here, the beam spot size is defined as the full width at half maximum (FWHM) of the E-intensity, and the focusing efficiency is defined by taking the ratio between the optical power within the circular area (diameter = 4 × FWHM) at the focal spot and the incident optical power on the metalens. In addition, four metalenses with different focal lengths of 4.843, 10, 17.32, and 31.798 μm, corresponding to the NA values of 0.9, 0.7, 0.5, and 0.3, respectively, are simulated. The focal spot size and the focusing efficiency are recorded, as shown in Figure 2C. The focal spot size is found to be increasing as the focal length increases. Its value is close to $\frac{\lambda}{2 \cdot \mathrm{NA}}$, which indicates that the focusing approaches the diffraction limit. The focusing efficiency has a significant increase from 39.6% to 76.2% as the focal length increases from 4.843 to 31.798 μm, which conveys that the bending of the incident wave with larger angle (higher NA) induces higher loss. The trade-off between the focusing efficiency and the NA should be considered in metalens design based on the application requirements.

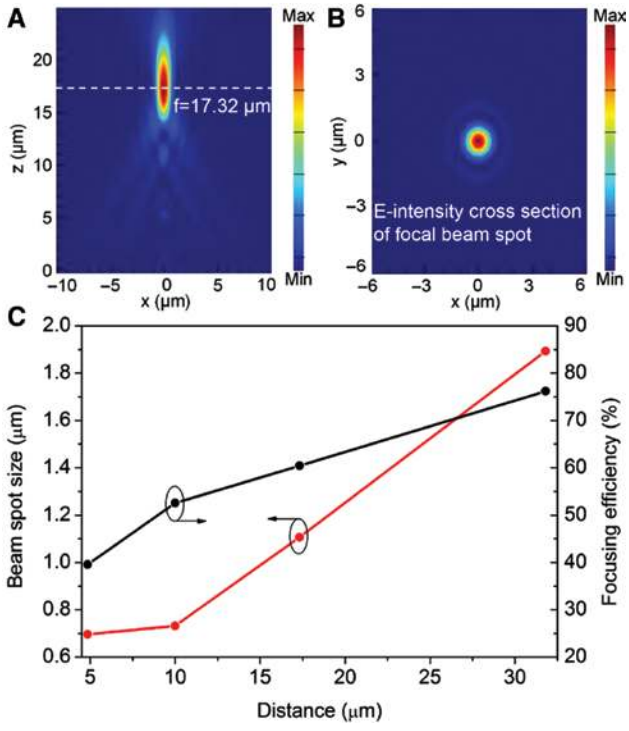

Figure 2: Simulation results of metalens.
Simulated E-intensity profile in (A) the propagation plane and (B) the focal plane of a 20-μm-diameter metalens with a focal length of 17.32 μm (NA = 0.5). (C) Simulated focal spot size and the focusing efficiency with respect to different focal lengths. The arrows indicate the corresponding y-axis of the data line.

3 Fabrication and characterization

In the layout, a 2-mm-diameter metalens with a focal length of 1.732 mm (NA = 0.5) was designed. The designed metalens is composed by nanopillars with a radial sampling distribution. The fabrication started with a standard 12-inch silicon wafer. A 1-μm-thick SiO_2 and a 600-nm-thick a-Si were deposited successively using the plasma-enhanced chemical vapor deposition method. Thereafter, 193-nm ArF DUV immersion lithography and inductively coupled plasma etch were used to make the a-Si pillars of the metalens. In the etch process, spin-on carbon was used as the hard mask. The patterned silicon wafer was covered by a 60-μm-thick interlayer of glue (siloxane) through spin coating. Then, it was bonded with a 12-inch glass wafer (SG3.4, Corning Specialty Materials Incorporated, New York, NY, US), followed by grinding and polishing from the backside of the silicon wafer to thin down the wafer thickness to ~20 μm. The remaining Si was then removed by wet etching using the SiO_2 layer as the stopping layer. Using this method, the patterned layer on the silicon wafer was transferred to the glass wafer. Figure 3A shows the photograph of the fabricated wafer. Most of the area is without pattern and hence transparent, through which the A*STAR logo (blue color) placed at the back can be visualized. The zoomed-in view of the central die is presented at the bottom part of Figure 3A, with the designed metalens highlighted in red-dotted line.

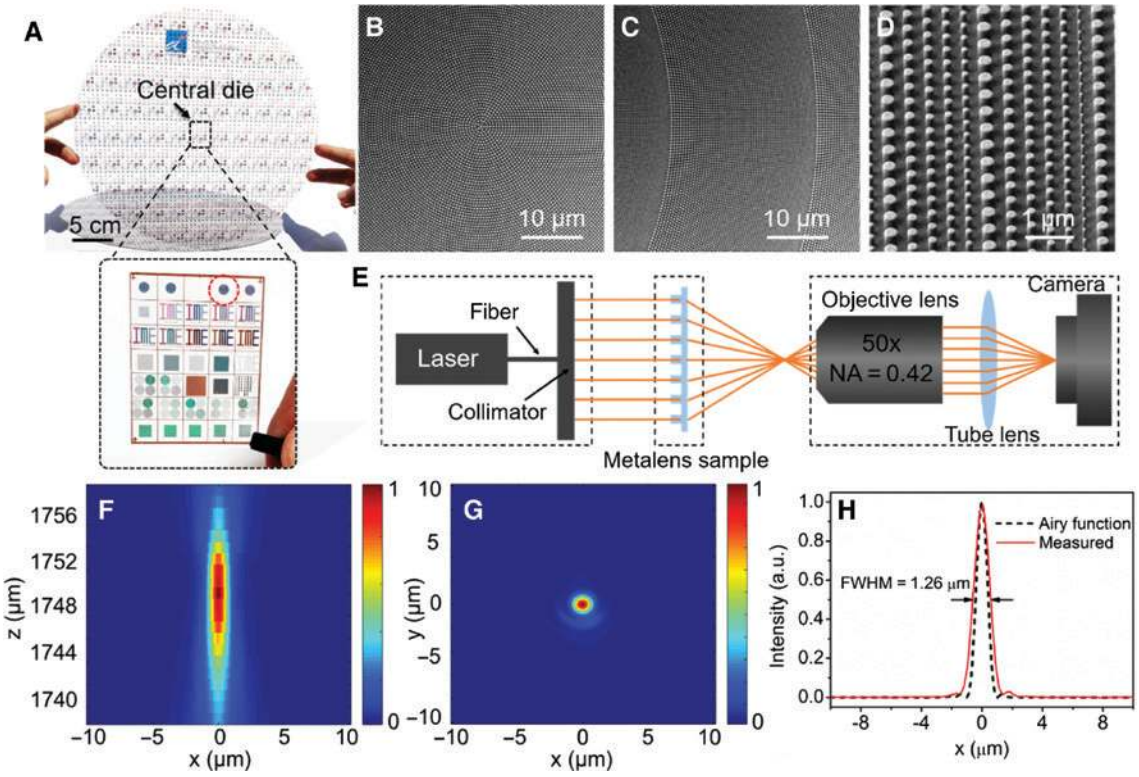

Figure 3: Characterization of the metalens fabricated on a 12-inch glass wafer.
(A) Color photographs of the fabricated 12-inch glass wafer and the central die in the wafer with highlighted area indicating the metalens. SEM images at the (B) central, (C) near-central, and (D) outer zones of the metalens. (E) Schematic of the metalens characterization setup (not to scale). Measured optical intensity of the metalens at the optical (F) propagation plane and (G) focal plane. (H) Horizontal cut of the focal spot shown in (G). An ideal Airy function with aperture of 2 mm and focal length of 1.75 mm is overlaid.

The flat optic devices with design variations and different functionalities are also included in the same die. Panels B and C of Figure 3 show the top-view scanning electron microscopy (SEM) images of the central and near-central zones of the metalens, respectively. Figure 3D shows a zoomed-in angled-view SEM image of the pillars close to the edge of the metalens. The diameters of these pillars change from large to small values to cover the phase shift from 0 to 2π. All the pillars in this image, including the ones with 100-nm diameter (the second column counting from right), have a straight and smooth side wall. It verifies the quality of the lithography and etching process.

The schematic of the metalens characterization setup is shown in Figure 3E. The 940-nm laser diode has a fiber pigtail connected to a fiber collimator. The collimated light, with a Gaussian intensity profile, incidents onto the metalens and then converges to a focal spot, which is later magnified by the objective lens (NA = 0.42, 50× magnification) and the tube lens. A camera is used at the end to capture multiple magnified optical profiles orthogonal to light propagation direction. The measured intensity distribution of the propagation plane is shown in Figure 3F, from which the focal length extracted is around 1.75 mm, corresponding to an NA of 0.496. The focal length deviates a little from the designed value of 1.73 mm. This may be attributed to the dimension drift and defects of the a-Si pillars induced during the fabrication process. The intensity profile at the focal plane is shown in Figure 3G. It can be observed that the light beam is focused to a spot at the center of the focal plane. Based on the definition mentioned in the device design, the focusing efficiency of the metalens is measured to be 29.2%, with the wafer transmission loss calibrated out. It is worth mentioning that the metalens has a higher NA than the objective lens used in the system, which causes additional loss during the measurement. Higher focusing efficiency can be obtained if the objective lens can be replaced by the one with a higher NA. To further analyze the focal spot, its intensity profile along the horizontal direction is plotted in Figure 3H. The spot size (FWHM) is found to be 1.26 μm. This is close to the 3D-FDTD simulation result of 1.08 μm shown in Figure 2C. An ideal Airy function with an aperture diameter of 2 mm and a focal length of 1.75 mm is also plotted in Figure 3H. Compared with the measured profile, the Airy function has a narrower line shape. This might be due to the fact that the intensity profile of the incident beam

has a Gaussian shape, and hence the incident intensity at the edge of the metalens is weaker compared with the central region. It leads to the decrease of the effective lens diameter and NA, and consequently, the increase of the focal spot size. The fabrication-induced error mentioned above is another factor affecting the beam size. Further optimization of the fabrication process and the measurement system (e.g. making the Gaussian intensity distribution flat) can achieve a focal spot closer to the ideal Airy function.

In order to apply the metalens in an imaging system, the characterization setup in Figure 3E is modified as shown in Figure 4A. An object is placed between the laser source and the metalens. The original objective lens is replaced by the one with 20× (or 50×) magnification and an NA of 0.4 (or 0.42). The 1951 USAF resolution test chart is used as the object. The image of the object is captured by the camera through a lens set. By controlling the relative position of the object and the metalens, the magnification of the image can be adjusted. The image of the resolution chart with the 14.7× and 33.8× magnification is recorded and shown in Figure 4B and C, respectively. As the image shown in Figure 4B, the lines in group 6 of the resolution chart can be captured clearly using the objective lens with 20× magnification. Using an objective lens with 50× magnification, the smallest element in group 7, which is also the smallest group in the resolution chart, with a line width of 2.19 μm is observed, as shown in Figure 4C. These results indicate that the imaging system with the metalens is able to capture images with a resolution of 228.1 lp/mm. Thus, it can be used to scan the fingerprint, which has a typical texture width of tens of micrometers.

A fingerprint image sample is then placed in front of the metalens to replace the resolution chart as the object. The laser source is also replaced by a 940-nm light-emitting diode with a relatively larger illumination area. In order to obtain a fingerprint image with a larger field of view, an objective lens with 5× magnification is used in place of the 20× or 50× one in Figure 4A.

The simplified schematic of a fingerprint imaging module with a single metalens is illustrated in Figure 5A. The relation among the object distance d, the image distance d_1, and the focal length f can be expressed in the following equation:

$$\frac{1}{f}=\frac{1}{d}+\frac{1}{d_1}. \tag{2}$$

Thus, the module thickness H_m can be expressed as

$$H_m = d + d_1 = \frac{dd_1}{f}. \tag{3}$$

For a lens with fixed focal length f and image distance d_1, the module thickness H_m can be reduced by reducing the object distance d. As a result, the view of the fingerprint area (FA) will decrease. To make the module thin and compact, while still keeping a sufficient FA, the metalens array can be used. The schematic of the fingerprint capturing system with metalens array is shown in Figure 5B. The whole fingerprint image can be obtained by combining the

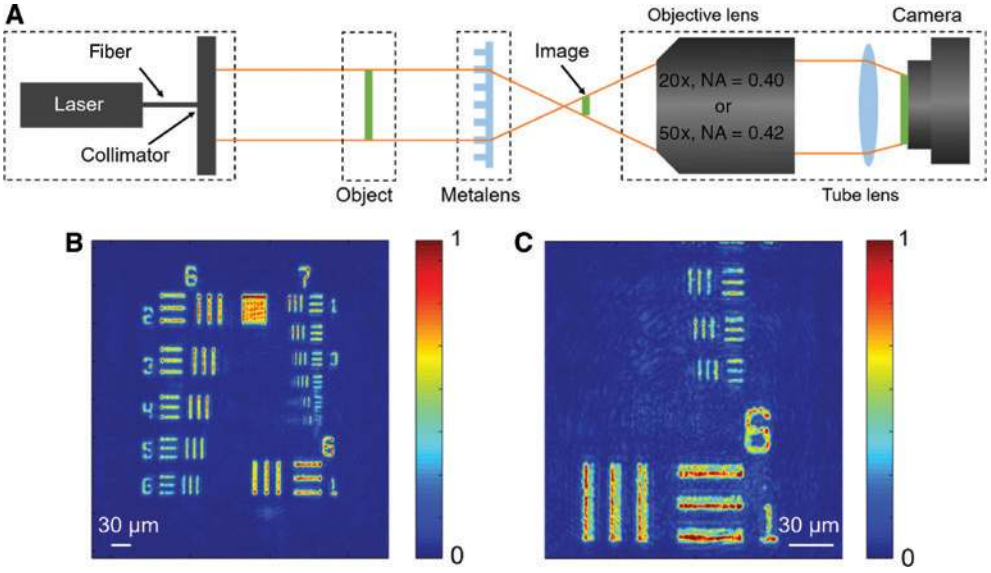

Figure 4: Metalens imaging system setup and results.
(A) Schematic of the imaging system setup, including the metalens. Image of the 1951 USAF resolution chart with (B) 14.7× and (C) 33.8× magnification.

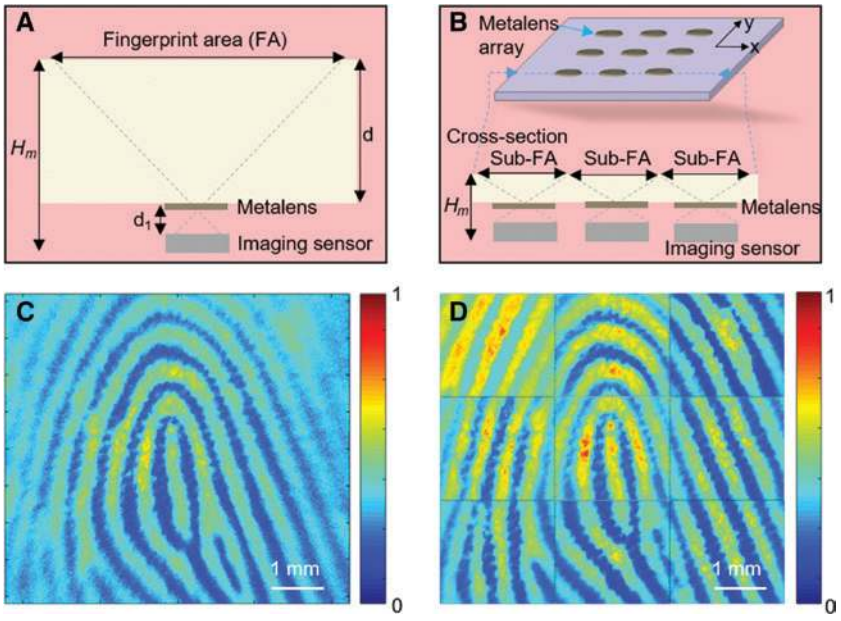

Figure 5: Fingerprint imaging demonstration with the fabricated metalens.
Schematic of the optical fingerprint system with (A) a single metalens and (B) a metalens array. (C) Captured fingerprint image using a single fixed metalens with single shot. (D) Combined fingerprint image by moving the location of the metalens for the proof-of-concept metalens array demonstration.

sub-FA captured by each metalens unit. Please note that panels A and B of Figure 5 are just to illustrate the idea of reducing module thickness by using metalens array in replacement of a single metalens.

For proof-of-concept demonstration, an image of a sub-FA is captured by the single metalens using the setup shown in Figure 4A, with a measured magnification of 3.195. As the camera has a pixel (size of 3.69 μm/pixel) number of 1928×1448 in the *x* and *y* directions, respectively, the location of the single metalens is programmed to move with the step of 2.23 mm (1928×3.69/3.195 μm) in the *x* direction and 1.67 mm (1448×3.69/3.195 μm) in the *y* direction in order to capture a 3×3 image array. The fingerprint images captured by a fixed metalens (with magnification of ~1) and by moving the metalens are shown in Figure 5C and D, respectively. It can be observed that the fingerprint textures at the edge of the combined image captured by moving the metalens with multiple shots is clearer than that captured by a fixed metalens with a single shot. This is due to the fact that the field of view is limited by the monochromatic aberrations [10]. The proposed metalens array scheme alleviates this problem, as a smaller field of view is required for each unit lens. In addition, the optical module thickness H_m with the single fixed metalens calculated using Eq. (2) and (3) is 11.86 mm, while this value with the idea of metalens array is 7.35 mm. Thus, the metalens-array-based optical fingerprint module not only improves the image quality but also makes the system more compact. It is worth noticing that the 3×3 image array obtained by moving the single metalens is not exactly equivalent to that captured by a 3×3 metalens array. In our experiment, considering the field of view of the camera, we calculate the moving step (2.23 mm in the *x* direction and 1.67 mm in the *y* direction) of the single metalens to avoid the overlap between sub-images in the stitched 3×3 image array. In reality, if a 3×3 metalens array with the same pitch size as the moving step is used to capture the fingerprint, there will be overlap and crosstalk between the sub-images. The design of metalens diameter and array pitch needs to be optimized to minimize/eliminate such crosstalk. Moreover, a software with robust algorithm can be used to reduce the influence of the crosstalk. By using such software together with optimized metalens array, a high-quality fingerprint image can be obtained. The optical fingerprint capturing module could be compact with a thickness of <1 mm by appropriately designing the metalens array and using the backgrind process to thin down the wafers. With the advanced complementary metal-oxide-semiconductor (CMOS)-compatible fabrication facilities, the patterning of the large-area metalens array can be achieved using the 193-nm immersion photolithography technology.

4 Conclusion

The metalens working at 940 nm is designed by 3D-FDTD simulation and fabricated on a 12-inch glass wafer using

the CMOS-compatible technology. The NA and the focal spot size of the metalens are measured to be 0.496 and 1.26 μm, respectively, which match well with the simulation. The focusing efficiency should be larger than the measured value of 29.2%, as the NA of the objective lens used in the characterization setup is lower than that of the metalens. The metalens is applied in an imaging system for a resolution test. A clear image of the smallest bar with the width of 2.19 μm in the 1951 USAF resolution chart is obtained. The same imaging system with the metalens is used to capture the image of a fingerprint. As a proof-of-concept demonstration, the single metalens is programed to move in order to mimic the function of a 3×3 metalens array. The fingerprint images are captured for both fixed metalens with a single shot and moving metalens with multiple shots. The experiment results convey that the latter not only improves the image quality but also makes the system more compact. By appropriate design of the metalens array and using the backgrind process to thin down the wafers, the thickness of the optical fingerprint capturing module could be <1 mm, which has potential applications in compact consumer electronics. The 193-nm ArF DUV immersion lithography and the rest fabrication process developed for this work can be used to fabricate the metalens working at even shorter wavelengths, i.e. visible regime. This work provides a promising solution for the mass manufacturing of metasurface-based optical components on glass wafers using the CMOS-compatible technology.

Funding: RIE2020 Advanced Manufacturing and Engineering Domain's Core Funds: SERC Strategic Funds (A1818g0028).

Acknowledgment: The authors would like to thank Dr. Ying Lin for assistance on photolithography. The appreciation extends to Dr. Yuandong Gu and Dr. Stephanie Yang for the project initiation.

References

[1] Yu N, Capasso F. Flat optics with designer metasurfaces. Nat Mat 2014;13:139–50.
[2] Khorasaninejad M, Capasso F. Metalenses: versatile multifunctional photonic components. Science 2017;358:6367.
[3] Aieta F, Genevet P, Kats MA, et al. Aberration-free ultrathin flat lenses and axicons at telecom wavelengths based on plasmonic metasurfaces. Nano Lett 2012;12:4932–6.
[4] Wang S, Wu PC, Su V-C, et al. Broadband achromatic optical metasurface device. Nat Commun 2017;8:187.
[5] Avayu O, Almeida E, Prior Y, Ellenbogen T. Composite functional metasurfaces for multispectral achromatic optics. Nat Commun 2017;8:14992.
[6] Genevet P, Capasso F, Aieta F, Khorasaninejad M, Devlin R. Recent advances in planar optics: from plasmonic to dielectric metasurfaces. Optica 2017;4:139–52.
[7] Arbabi A, Horie Y, Bagheri M, Faraon A. Dielectric metasurfaces for complete control of phase and polarization with subwavelength spatial resolution and high transmission. Nat Nanotechnol 2015;10:937–44.
[8] Arbabi A, Horie Y, Ball AJ, Bagheri M, Faraon A. Subwavelength-thick lenses with high numerical apertures and large efficiency based on high-contrast transmitarrays. Nat Commun 2015;6:7069.
[9] Khorasaninejad M, Aieta F, Kanhaiya P, et al. Achromatic metasurface lens at telecommunication wavelengths. Nano Lett 2015;15:5358–62.
[10] Arbabi A, Arbabi E, Kamali SM, Horie Y, Han S, Faraon A. Miniature optical planar camera based on a wide-angle metasurface doublet corrected for monochromatic aberrations. Nat Commun 2016;7:13682.
[11] Arbabi E, Arbabi A, Kamali SM, Horie Y, Faraon A. Multiwavelength polarization-insensitive lenses based on dielectric metasurfaces with meta-molecules. Optica 2016;3:628–33.
[12] She A, Zhang S, Shian S, Clarke DR, Capasso F. Large area metalenses: design, characterization, and mass manufacturing. Opt Express 2018;26:1573–85.
[13] Park J-S, Zhang S, She A, Chen W-T, Yousef KMA, Capasso F. Large-area, single material metalens in the visible: an approach for mass-production using conventional semiconductor manufacturing techniques. In: OSA Conference on Lasers and Electro-Optics (CLEO), 2019:STh1O.5.
[14] Khorasaninejad M, Chen WT, Zhu AY, et al. Multispectral chiral imaging with a metalens. Nano Lett 2016;16:4595–600.
[15] Khorasaninejad M, Chen WT, Devlin RC, Oh J, Zhu AY, Capass F. Metalenses at visible wavelengths: diffraction-limited focusing and subwavelength resolution imaging. Science 2016;352:1190–4.
[16] Khorasaninejad M, Zhu AY, Carmes CR, et al. Polarization-insensitive metalenses at visible wavelengths. Nano Lett 2016;16:7229–34.
[17] Chen WT, Zhu AY, Sanjeev V, et al. A broadband achromatic metalens for focusing and imaging in the visible. Nat Nanotechnol 2018;13:220–6.
[18] Chen BH, Wu PC, Su V-C, et al. GaN metalens for pixel-level full-color routing at visible light. Nano Lett 2017;17:6345–52.
[19] Wang S, Wu PC, Su V-C, et al. A broadband achromatic metalens in the visible. Nat Nanotechnol 2018;13:227–32.
[20] Zhan A, Colburn S, Trivedi R, Fryett TK, Dodson CM, Majumdar A. Low-contrast dielectric metasurface optics. ACS Photonics 2016;3:209–14.
[21] Domínguez RP, Yu YF, Khaidarov E, et al. A metalens with a near-unity numerical aperture. Nano Lett 2018;18:2124–32.
[22] Lin D, Fan P, Hasman E, Brongersma ML. Dielectric gradient metasurface optical elements. Science 2014;345:298–302.
[23] Bai W, Yang P, Huang J, et al. Near-infrared tunable metalens based on phase change material $Ge_2Se_2Te_5$. Sci Rep 2019;9:5368.
[24] Liu M, Fan Q, Yu L, Xu T. Polarization-independent infrared micro-lens array based on all-silicon metasurfaces. Opt Express 2019;27:10738–44.
[25] Yang T, Liu Y-H, Mu Q, et al. Compact compound-eye imaging module based on the phase diffractive microlens array for biometric fingerprint capturing. Opt. Express 2019;27:7513–22.

[26] Hu T, Tseng C-K, Fu YH, et al. Demonstration of color display metasurfaces via immersion lithography on a 12-inch silicon wafer. Opt Express 2018;26:19548–54.
[27] Xu Z, Dong Y, Tseng C-K, et al. CMOS-compatible all-Si metasurface polarizing bandpass filters on 12-inch wafers. Opt Express 2019;27:26060–9.
[28] Zhong Q, Li Y, Hu T, et al. 1550nm-wavelength metalens demonstrated on 12-inch Si CMOS platform. In: IEEE 16th International Conference on Group IV Photonics (GFP), 2019:1949–209X.
[29] Dong Y, Xu Z, Li N, et al. Si metasurface half-wave plates demonstrated on a 12-inch CMOS platform. Nanophotonics 2019;9:149–57.
[30] Li N, Fu HY, Dong Y, et al. Large-area pixelated metasurface beam deflector on a 12-inch glass wafer for random point generation. Nanophotonics 2019;8:1855–61.
[31] Xu Z, Dong Y, Fu YH, et al. Embedded dielectric metasurface based subtractive color filter on a 300mm glass wafer. In: Conference on Lasers and Electro-Optics, OSA Technical Digest. Optical Society of America, 2019:STh1O.4.